

INTERNATIONAL JOURNAL OF SCIENTIFIC AND UNIVERSITY RESEARCH PUBLICATION

International Journal Of Scientific And University Research Publication

ISSN No 311/714

Listed & Index with ISSN Directory, Paris



Multi-Subject Journal



Volum : (16) | Issue : 210 |

Research Paper



NEAR REAL-TIME WILDFIRE PROGRESSION MONITORING WITH SENTINEL-1 SAR TIME SERIES AND DEEP LEARNING

Yifang Ban || Division of Geoinformatics

KTH Royal Institute of Technology

10044

Stockholm

Sweden

In recent years, the world witnessed many devastating wildfires that resulted in destructive hu environmental impacts across the globe. Emergency response and rapid response

ملخص

for mitigation calls for effective approaches for near real-time wildfire monitoring. Capable of penetrating clouds and smoke, and imaging day and night, Synthetic Aperture Radar (SAR) can play a critical role in wildfire monitoring. In this communication, we investigated and demonstrated the potential of Sentinel-1 SAR time series with a deep learning framework for near real-time wildfire progression monitoring. The deep learning framework, based on a Convolutional Neural Network (CNN), is developed to detect burnt areas automatically using every new SAR image acquired during the wildfires and by exploiting all available pre-fire SAR time series to characterize the temporal backscatter variations. The results show that Sentinel-1 SAR backscatter can detect wildfires and capture their temporal progression as demonstrated for three large and impactful wildfires: the 2017 Elephant Hill Fire in British Columbia, Canada, the 2018 Camp Fire in California, USA, and the 2019 Chuckegg Creek Fire in northern Alberta, Canada. Compared to the traditional log-ratio operator, CNN-based deep learning framework can better distinguish burnt areas with higher accuracy. These findings demonstrate that spaceborne SAR time series with deep learning can play a significant role for near real-time wildfire monitoring when the data becomes available at daily and hourly intervals with the launches of RADARSAT Constellation Missions in 2019, and SAR CubeSat constellations.

Yifang Ban would like to KTH Royal Institute of Technology for the

7 ...

Research shows that human-induced climate changes have led to hot, dry conditions that increase the outbreaks of wildfires in various . In both 2017 and 2018, the world witnessed many ¹regions devastating wildfires. Hotter summers and drought across northern Europe and North America have resulted in increased wildfire activity in cooler and wetter regions such as Sweden, even north of the Arctic Circle. During the summer of 2018, Sweden experienced an exceptionally long period of drought resulting in over 50 forest fires. In British Columbia, Canada, a total of 2,092 wildfires burnt more than 1.3 million hectares of land in 2018, while in California, USA, a total of 8,527 wildfires burned an area of 800 000 hectares, the deadliest and most destructive wildfire season in California's history. Early identification of the location and size of these fires can inform fire-fighting operations at an early stage. Moreover, being able to monitor wildfire progression and burnt areas in both cloudy and smoky conditions as well as during day and night would increase the information base for decision-making and improve the speed and efficiency for wildfire emergency response. With its synoptic view and large area coverage at regular revisits, satellite remote sensing has long played a crucial role in disaster management including wildfire. Owing to the rapid development of satellite technology, we are moving forward to a new era of Earth Observation (EO). National and International space agencies, as well as innovative companies have started various EO programs that are able to acquire massive amounts of satellite imagery with increasingly higher spatial resolution and rapid temporal intervals. With the recent launches of the European Space Agency (ESA)'s Sentinel-1 and Sentinel-2 satellites, SAR and optical data with global coverage and frequent revisits have become freely available. These open EO big data represent a great opportunity to develop innovative methodologies for near real-time wildfire monitoring. The main challenge is the lack of robust and automated methods to extract relevant information from such massive amounts of EO data.

For active wildfire monitoring, the low spatial resolution Visible Infrared Imaging Radiometer Suite (VIIRS) and the Moderate Resolution Imaging Spectroradiometer (MODIS) are often used for preliminary mapping and contextual awareness while Landsat and Sentinel-2 data are deployed for post-fire boundary determination . Optical images at critical time frame, ^{2,3,4,5} and burn severity mapping

however, are often unavailable due to frequent cloud cover in the . As an active sensing technology, not ⁶boreal and tropical regions relying on solar radiation, SAR is capable of penetrating clouds and . As a result, SAR has been ⁷smoke as well as imaging day and night playing an increasingly important role in environmental change -monitoring. Past studies evaluated various SAR data at X-, C-, and L bands in different polarizations for burnt area mapping and burn -. For examples, Bourgeau-8,9,10,11,12,13,14,15,16,17 severity estimation - evaluated European remote sensing satellite (ERS) C-¹⁷havez et al. and SAR for detection of boreal fire scars in various boreal ecosystems globally was possible using C-band SAR data. Gimeno et al., identified burnt areas in Mediterranean forests using Principle ¹⁸Component Analysis (PCA) and neural network classification Polychronki et al. evaluated Advanced Land Observing Satellite (ALOS) the Phased Array type L-band Synthetic Aperture Radar (PALSAR) imagery for burnt area mapping using an object-based . Tanase et al. investigated spaceborne X-, ¹³classification in Greece C- and L-band co- and cross-polarized data for burn severity . Previous results reported a ¹⁶estimation in Spanish pine forests substantial decrease of the C-band VH backscatter in fire-disturbed forests and demonstrated the effectiveness of cross-polarized SAR -. Conversely, several C-band SAR-11,19 for detection of burn scars ased studies revealed an increase in co-polarized backscatter from fire-disturbed forests in boreal and Mediterranean due to rain-fall . As a result of the ^{10,13,14,15,17,20,21} events and low evapotranspiration partial or complete removal of forest canopy, changes in the soil moisture have a significant effect on SAR backscatter. C-band SAR backscatter from fire scars were observed to 3-6 dB higher than the

The capability of Sentinel-1 for fire scar mapping was investigated in . According to Imperatore et ^{8,11,24}recent studies with mixed results , there is an obvious change in VH backscatter for the burnt area ¹¹al. -dominated by forests, thus, permitting the delineation of the fire affected areas. However, the detection of the burnt areas for grass and non-forest vegetation is more complex. C-band SAR backscatter of burnt grass is similar to that of dry grass. The main challenges of using SAR for detecting burnt areas and mapping fire scars are

adjacent unburnt forest in Alaska when the soil was wet. Similar

backscatter behaviors caused by soil moisture changes were also

observed in fire-disturbed forests in various environmental conditions

around the world, including Australia, Canada, Indonesia, the . $^{17,18,20,22,23}_{}$ Mediterranean and Siberia

evacuations and burnt an estimated 192,000 hectares of forest. The

notably large fire burned from Ashcroft and Cache Creek in the

southwest, north to Clinton and further northwest, then over to Sheridan Lake in the northeast and south along the margin of the

Deadman Valley. The region is sparsely populated and has complex terrain with limited access capability. The elevations in the area range

from 278 m to 1785 m with a mean elevation of 1142 m and a

standard deviation of 224.9 m. Further relating the topographic

complexity of the terrain, the slopes vary from 0° to 71° with the

mean slope of 8.1° and standard deviation of 6.85°. The major land

cover classes include forest, grassland, clear cuts, barren land and

The Camp Fire was the deadliest and most destructive wildfire in California history. Started on November 8 near Camp Creek Road in

Butte County, northern California and contained on November 25,

2018, the fire caused at least 85 civilian fatalities, 3 missing and 17

injured, and the evacuation of 52000 people. The fire also destroyed 18804 structures and burnt over 62000 hectares. The area is located

in the foothills of the Sierra Nevada and the Sierra Nevada mountain

range in the western United States. Compared to Elephant Hill, this

region has steep complex mountainous terrain. The elevations in the

area range from 49 m to 1569 m with a mean elevation of 551 m and

a standard deviation of 325 m. The slopes vary from 0° to 72° . The mean slope is 14.6° , double that of the Elephant Hill, with a standard

deviation at 9.91°. The major land cover types include forest,

The Chuckegg Creek Fire, located west of High Level, was the

largest forest fire in Alberta in 2019. Started on May 17, 2019 and

contained on July 26, 2019, the fire burned an estimated 350,134

hectares of vegetation. Compared to the above two study areas, the

terrain in the region is less complex and relatively flat. The elevations in the area range from 248 m to 796 m with a mean elevation of

375.5 m and a standard deviation of 55.4 m. The corresponding

slopes vary from 0° to 60° with a mean slope of 2.25° and a standard deviation of 2.06°. The major land covers include forest, shrubland,

grassland, wetland and barren land. The geography and topography of

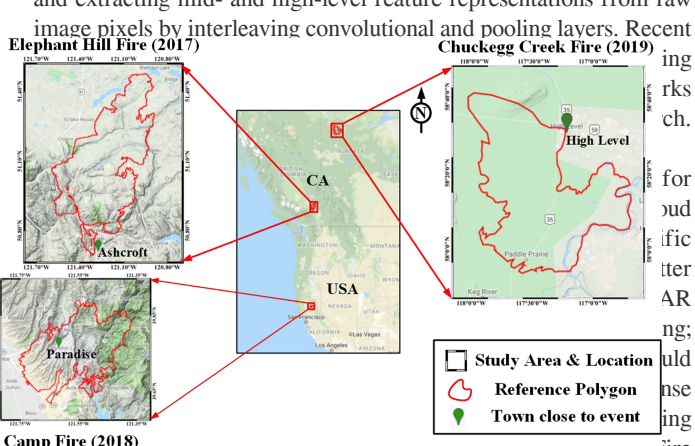
grassland, barren land, crop land and settlements.

the three study areas are shown in Fig. 1.

settlements.

related to the complex interactions of SAR system parameters, including frequency, polarization, incidence angles and look direction, and land surface parameters, including geometric properties (type and structure, surface roughness, geometry and topography etc.) and dielectric properties (i.e., surface moisture), as well as environmental conditions (e.g., rain, dew, wind etc.). Therefore, further research is needed to better understand the temporal backscatter behavior of Sentinel-1 C-Band SAR in VV and VH polarizations for burnt forest and grassland compared to that of burnt areas. Spaceborne SAR data and their fusion with Landsat data were also investigated for near-real time deforestation . To the best of our knowledge, however, no study 25,26,27 monitoring was found on SAR for wildfire progression monitoring. Therefore, it is desirable to investigate Sentinel-1 SAR dense time series data for wildfire progression monitoring. Wildfires burn vegetation thus result in changes in the SAR backscatter intensity that can be identified with change detection.

Change detection has been used successfully in many diverse -applications, including monitoring environmental changes, land use/land-cover dynamics, deforestation, disaster damage, and . Various change detection techniques have $^{28,29,30,31,32,33} urbanization \,$, ³⁵, Bazi et al. ³⁴been developed, such as those by Bruzzone and Prieto . However, most of these ³⁷ and Bovolo et al. ³⁶Bovolo and Bruzzone methods and algorithms were developed considering the availability of a few or just two images (pre- and post-event) that can be used to detect the changes. Change detection remains a challenging task using SAR data due to complexity of wildfire affected forest environment. Some of the common issues of change detection, however, could be resolved by exploiting the high temporal resolution of Sentinel-1 time series using the highly redundant information following the big data paradigm. The idea is to exploit the temporal fluctuations of the remotely sensed measurements to remove the confusion between burnt areas and other changes. As one of the fastest-growing trends in big data analytics, deep learning is proving to be a very effective and semantic 38,39,40 technique for large-scale image recognition . Among deep learning models, the most exciting is $\frac{41}{5}$ segmentation the potential of CNN in learning complex non-linear transformation and extracting mid- and high-level feature representations from raw



Camp Fire (2018) In unce different study areas, the Elephant Tim Fire (2017) in British Columbia of Canada, the Camp Fire (2018) in California, U.S.A., and the Chuckegg Creek Fire (2019) in northern Alberta of Canada.

Data description

Sentinel-1 SAR data

The Sentinel-1 mission, the first of European Space Agency's five Copernicus Missions, is a constellation of two polar-orbiting satellites -launched on April 3, 2014 and April 25, 2016 respectively. The C band Synthetic Aperture Radar (SAR) operates day and night in dual polarizations and acquires imagery continuously regardless of (ESA, 2019). In this study, ⁴⁶weather with a 6-day revisit at equator all available Sentinel-1 SAR C-band time series data in VV and HV

Study Areas and Data Description Study areas

Three recent wildfires, the Elephant Hill wildfire (Canada, 2017), the Camp Fire (U.S.A., 2018) and the Chuckegg Creek Fire (Canada, 2019), were selected for this research to represent different environmental conditions. The Elephant Hill wildfire (Canada) was British Columbia's largest wildfire in 2017. Started on July 6 along the Thompson River near Ashcroft and contained in mid-September, 2017, the fire destroyed over 300 buildings, prompted mass

IF: 4.176 | IC Value: 78.46

BR=NIR-SWIR2NIR+SWIR2 NBR=NIR-SWIR2NIR+SWIR2

polarizations, acquired in Interferometric Wide Swath (IW) mode, were collected for the Elephant Hill Fire, Camp Fire and Chuckegg Creek Fire sites during 2017, 2018 and 2019 respectively. , the ⁴⁷Downloaded from the Google Earth Engine (GEE) Platform Level 1 Ground Range Detected (GRD) products consist of focused SAR data that has been detected, multi-looked and projected to ground range using an Earth ellipsoid model. The SAR data were then terrain corrected converted to decibels (dB) via log scaling.

(1)

Reference data

High resolution Worldview-3 post-fire imagery over the Elephant Hill Fire site was acquired on September 28, 2017 and used to visually verify the SAR-based burnt area maps. Fieldwork was also conducted in the Elephant Hill Fire area in July, 2018, one-year after the wildfire. Ground at a representing various burn severities were collected by field inspection and with a drone. Figure 2 shows various burn severities under different terrain conditions.





d

NBRpre-fire-NBRpost-fire dNBR=NBRpre-fire-NBRpost-fire

(2)

To better understand the behavior of SAR temporal backscatter under different conditions, precipitation data over the study areas was collected. For the Elephant Hill Fire, the precipitation data used is PERSIANN-CDR, a daily precipitation estimation from remotely sensed information with artificial neural network-Climate Data For the Camp Fire, ^{49,50}Record, at a resolution of 0.25 arc degrees the precipitation data is from the Climate Hazards Group InfraRed -Precipitation with Station data (CHIRPS), which is a 30 year quasi global daily rainfall dataset and it incorporates 0.05° resolution .51 satellite imagery with in-situ station data

Results and Discussion

Sentinel-1 SAR temporal backscatter patterns of burnt and unburnt vegetation

To better understand the SAR backscatter behaviors of burnt and unburnt vegetation, several areas of interest (AOI) on SAR time -series representing forest and grassland in similar vegetation (pre fire) and topographic conditions (elevation, slope, aspect) were selected for analysis and comparison of their temporal backscatter patterns. The SAR backscatter statistics corresponding to several comparable pairs of AOIs for burnt and unburnt forest and grassland is presented in Table 1. For each AOI, the location, size and topographic information as well as their temporal means and standard deviations of SAR backscatter are listed. The reason why we use differently sized AOIs for these two fire events is that the terrain of the Camp Fire is much more complex and locally dynamic than that of the Elephant Hill Fire. Therefore, the smaller AOIs are more

homogenous and representative

	nomogenous una representative.						
	Land	Cover	Fire Event				
			long. (°)				
\vdash	1 .	6 .	El l TI'll				
	unburnt	forest	Elephant Hill				

To verify and validate the SAR-based mapping results, cloud-free Sentinel-2 Multispectral Instrument (MSI) imagery before, during, and after the wildfires were selected in the Elephant Hill Fire in 2017, the Camp Fire in 2018 and the Chuckegg Creek Fire in 2019. For validation, burnt areas were automatic extracted using pre-fire and post-fire Normalized Burn Ratio (NBR) and their difference . For each study area, the ⁴⁸(denoted as dNBR) using Eqs. (1) and (2) accuracy of the SAR-based final burnt area map was quantitatively assessed using 20,000 validation points (10,000 points each for burnt and unburnt areas respectively) randomly selected based on the burnt area map derived from the post-fire Sentinel-2 imagery. It should be noted that the randomly selected training and validation data sets are from the same geographical region. Therefore there is a slight chance that a few of the validation samples overlap or in close vicinity of the training samples. This may affect the overall accuracy of the mapping results. Due to lack of ground truth data during the wildfires and no Sentinel-2 or Landsat imagery to couple with each SAR acquisition during the wildfires, the SAR-based progression maps were visually compared with the burnt area maps that were derived from Sentinel-2 imagery acquired right after each acquisition date of the SAR data.

C-VH (dB)	Land Chopergraphy	A G Ire Event	Land Cover	Fire Event long. (°)	
elevation(m)	size (m)	lat. (fi)ng. (°)			
			60 (ASC-64)		

IF: 4.176	IC Value :	78.46
-----------	------------	-------

C-VH (dB)	Topography	AOI		Land Cover		Fire Event	
elevation(m)	size (m)	lat. (°)				long. (°)	
				121.35W	burnt		
5.12	790	50.69N		121.38W	unburnt	grass	
5.36	748	50.75N		121.33W	burnt		
100	20.72N	121 20W			Canada	Come E'm	
100	39.73N	121.38W		unburnt	forest	Camp Fire (ASC-137)	
						(150 157)	
5.06	729	39.79N		121.53W		burnt	
5.68SAR backs	scatter variels 70 ver time in	four pair39f7 5N burnt and	burnt	121.76W	unburnt	grass	
	h of which are with simil						
	OIs atype. SAR backscatte						
	Is in the Elephant Hill bi			121.70W	burnt		
) Grass d)	Forest AOIs in the Camp	fire (ASC-137). (c(ASC-	64). (
	AC	Is in the Camp fire (ASC-	137).				

For the grassland AOIs in the Elephant Hill Fire site, similar temporal backscatter patterns to forest are observed, as shown in Fig. 3(b). The mean backscatters of the burnt AOI decreased while that of unburnt AOI remain relatively stable. Again, the precipitation events did not affect the SAR backscatter as the rain events were not right before the SAR data acquisitions. For the grassland AOIs in the Camp Fire site, as shown in Fig. 3(d), obvious increases in C-VV backscatters after the start of the wildfire are observed due to rain events, similar to forest backscatter increase in the Camp Fire site. Several heavy rain events occurred between Nov. 21 and Nov. 28 of 2018, and VV is more sensitive to the soil moisture than VH in burnt areas. However, the C-VH backscatter patterns of unburnt and burnt grassland remain the same after the fire. The reasons for this need further investigation as C-band radar signature is usually not significantly influenced by dry grass subject to fire event according to literature. This observation further confirms the previous findings that identification of the burnt area for non-forest vegetation (i.e., grassland) is not so straightforward.

Sentinel-1 SAR for near real-time wildfire progression monitoring

Elephant hill fire

The SAR-based wildfire progression maps of the Elephant Hill Fire are presented in Fig. 4, estimated by different methods, including the , the ratio between the logRt and the ³⁵classical log-ratio (logRt) corresponding historical stdDev map (kmap) and CNN-based framework. The first three rows show the estimated change maps, while the fourth row shows the binary progression maps corresponding to the burn confidence maps predicted by CNN in the third row. Row 5, labeled as CNN_mrg, presents the merged progression maps for each date, produced by accumulating all the progression maps before a date. To reduce unnecessary noises, the merging operation was not applied on the first two dates, i.e., July 8 and July 20, 2017. In the last row, CNN_tsc_mrg denotes that a

The examples of the SAR temporal backscatter behaviors of burnt and unburnt forest and grassland, corresponding to the AOIs listed in Table 1 and shown in Fig. 3. For each pair of the AOIs, the daily precipitation histograms are also shown in this figure since vegetation wetness and soil moisture conditions could impact the SAR backscatter. Figure 3(a,b) show the SAR backscatter variations over time for forest and grassland respectively in Elephant Hill Fire site while (c) and (d) display the temporal backscatter variations in the Camp Fire site. Figure 3(a) shows that, before the wildfire event on July 6, 2017, the AOIs of burnt and unburnt forest share the same SAR backscatter patterns, indicating that the forested areas have very similar vegetation and topographic conditions before the fire. After July 6th, however, the mean backscatters for both C-VH and C-VV polarization in the burnt AOI decreased approximately 2-3.5 dBs, with a larger standard deviation while the SAR mean backscatters in the unburnt AOI remain rather stable. The temporal trends of C-HVs and C-VV backscatter are very similar even though C-VV backscatter coefficients are several dBs higher than that of C-VH. The precipitation events did not affect the backscatter for either burnt or unburnt forest as the rain events were not right before the SAR data acquisitions. Similarly, burnt AOI shares similar backscatter patterns to unburnt AOI before fire in the forest AOIs of the Camp Fire site. However, both C-VV and C-VH backscatter coefficients increased after the fire event, as shown in Fig. 3(c). The increase in backscatter of burnt forest is likely caused by rain events immediately before the SAR data acquisitions resulting in higher soil moisture contents in burnt areas.

Figure 3

0.760678 84067937%	03%34 0 4	slogRW	H S1				
		0.7277	0.5553	77.78	93.86	59.42	VV
				%	%	%	
	0.7480	0.5939	79.70	98.53	60.92	kmap	VH
			%	%	%		
	0.7264	0.5633	78.17	97.23	57.98		VV
			%	%	%		
0.8884	0.7899	89.50	94.71	83.66	>2	kmap	VH,
		%	%	%			VV
9467.0	8983.0	.94	93.36	.90	Otsu	CNN_	VH,
		92%	%	41%		mrg	VV
0.9221	0.8548	92.74	.99	85.89		CNN_t	
		%	52%	%		sc_mr	
						g	

Due to lack of field data and optical images acquired on the same date as the SAR imagery during the wildfire, the progression maps are validated visually by overlaying CNN_mrg on the Sentinel-2 false). For each $_2,\,B=SWIR_1,\,G=SWIR_2color$ composite (R = SWIR map in CNN_mrg_overlay, the Sentinel-2 image with the closest cloud-free date after the SAR acquisition. Visual observation shows that there is a high level of agreement between Sentinel-1 SAR progression map and Sentinel 2 burnt area in the full time series. The examples of the overlays are presented in Fig. 5.

simple time series correction (TSC) was applied on the progression maps in the same orbit before merging them. It is assumed the burnt area would not disappear in the later progression once it appeared before, TSC can be used to reduce the noisy pixels in the earlier progression maps based on the later progression maps. However, with TSC, the CNN_tsc_mrg is not a near real-time approach any longer because it depends the future progression maps. For any date in the Elephant Hill Fire, the TSC was implemented by multiplying it with the future progression maps in the same orbit.

Figure 4

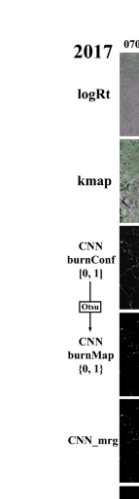
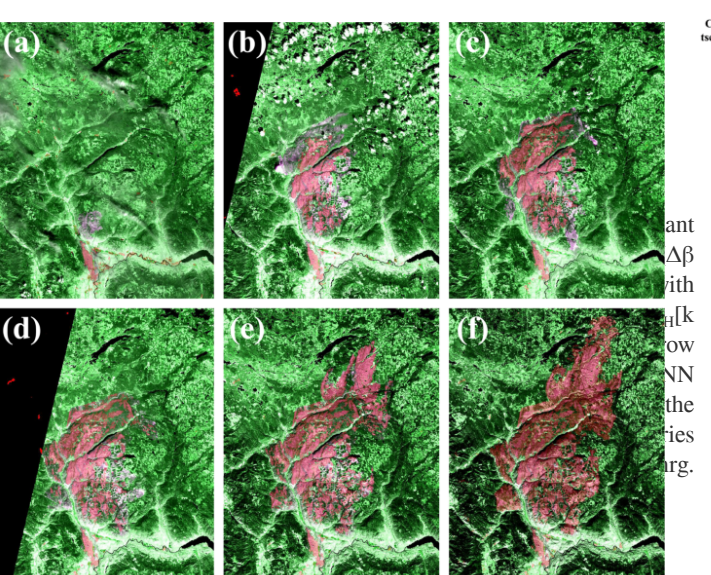


Figure 5



Full size image

To quantitatively assess SAR-based burnt area results, Sentinel-2 dNBR is segmented into a binary map of burnt and unburnt areas and used as the reference maps together field data and WorldView-3 imagery. 10,000 validation points are randomly selected from burnt and unburnt areas respectively. Table 2 presents the quantitative evaluation of SAR-based wildfire progression results for the Elephant Hill Fire. Among logRt, kmap, CNN_mrg and CNN_tsc_mrg, CNN_mrg achieves the highest , CNN_tsc_mrg ranks 1values in Precision, Recall, OA, Kappa and F-second, and both of them are much higher than logRt and kmap based results. It is worth noting that CNN_tsc_mrg reaches a very high value in Recall (0.9952), which implies that TSC greatly reduces the false alarm rate, compared to CNN_mrg's Recall (0.9336).



Fig

Sentinel-1 based wildfire progression maps in the Elephent Hill (CNN_mrg in transparent red) overlaid on the Sentinel-2 MSI false -) SAR-a). ($_2$, B = SWIR $_1$, G = SWIR $_2$ color composites (R = SWIR $_2$ -) SAR-c) SAR-July 20 on MSI-July 30. (buly 8 on MSI-July 10. ($_1$ -) SAR-e) SAR-Aug. 8 on MSI-Aug. 11. (dug. 1 on MSI-Aug. 4. ($_2$ -) SAR-Sept. 18 on MSI-Oct. 3. The imagesfug. 21 on MSI-Aug. 22. ($_2$ -)

were generated using Google Earth Engine platform (Map data: Google, ESA).

Full size image

In the first four stages, most of the burnt areas are in purple, indicating that VH backscatter is more sensitive than VV to the changes caused by the wildfire event, while the white pixels indicate that VH and VV show similar sensitivity to the changes. However, in the last four stages, the burnt area appears very different, in green instead of purple. The green pixels show that VV backscatter are more sensitive than VH to the fire-induced changes. This is because several heavy precipitations occurred between Nov. 21 and Nov. 28 of 2018, and VV is more sensitive to the soil moisture than VH in burnt areas. As shown in the CNN burnConf maps, the first two stages (a) and (b) indicate that CNN helps enhance the difference between burnt and unburnt areas, but significant over and under estimations are observed. As new SAR data comes, the CNN model is fine-tuned further, then the predicted CNN burnConf maps show much better contrast between burnt and unburnt pixels than the first two stages. With Gaussian filtering followed by Otsu , CNN burnConf maps in range [0, 1] are binarized 52thresholding into CNN burnMap. As expected, the first stage (a) looks rather noisy and the later stages detect most of the burnt areas with less noise. CNN_mrg combines all detected burnt areas on different orbits before current dates, except for the first date, Nov. 11, 2017, which is too noisy. CNN_tsc_mrg provides non near real-time results with less false alarm pixels by applying time series correction on the same orbit. By overlaying Senintel-1 SAR-based progression results (in transparent red) and Sentinel-2 SWIR composite, the bottom row demonstrates that there is a certain degree of agreement between Senintel-1 SAR-based progression maps and Senintel-2 fire scars. Compared to the visual observations in the Elephant Hill Fire, the agreement on the Camp Fire is not as good.

Quantitative evaluations of SAR-based wildfire progression results of the Camp Fire are presented in Table 3. With kmap, C-VV achieves score, and 1a much higher value than C-VH in OA, Kappa and F combining C-VV and C-VH can reach a higher accuracy than VV or VH alone. By combining VH and VV, CNN_mrg achieves an overall: 0.8139), 1accuracy of 83.58% (Kappa: 0.6716, F and CNN_tsc_mrg reaches a higher Recall value than CNN_mrg, i.e., a lower false alarm rate.

$_{1}F$	Kappa	OA	Recall	Precisi	Seg.	Metho	Data	Sat.
				on		d		
0.3269	0.1014	55.07	65.13	21.82	>2	kmap	VH	S1
		%	%	%				
0.5782	0.3404	67.02	80.19	45.21			VV	
		%	%	%				
0.6305	0.4002	70.01	82.11	51.17	>2	kmap	VH,	
		%	%	%			VV	
8139.0	6716.0	.83	93.91	.71	Otsu	CNN_	VH,	
		58%	%	82%		mrg	VV	
0.8103	0.6694	83.47	.95	70.60		CNN_t		
		%	07%	%		sc_mr		
						g		

Chuckegg creek fire

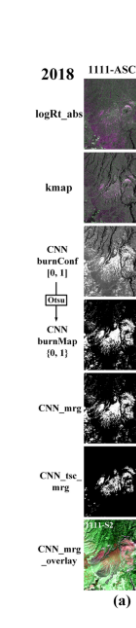
Figure 7 presents the SAR-based wildfire progression maps of the Chunkegg Creek Fire, estimated by logRt, kmap and the proposed CNN-based deep learning framework. Different from the Elephant Hill Fire and the Camp Fire, Sentinel-1 SAR acquired images every six days in the same orbit (ASC20) over the Chuckegg Creek Fire, a

Full size image

Camp fire

The SAR-based wildfire progression maps of the Camp Fire are presented in Fig. 6, estimated by different methods, including logRt with absolute operation (denoted as logRt_abs), kmap and CNN Confidence map (CNN burnConf). Compared with logRt_abs and kmap, we can find that CNN burnConf highlights the burnt areas very well, that is critical for subsequent segmentation. The row marked with CNN burnMap shows the corresponding binary ⁵²map of CNN burnConf maps with Otsu thresholding and CNN_mrg and CNN_tsc_mrg are produced with similar procedures for the Elephant Hill Fire. For the Camp Fire, the logRt_abs is exploited to detect both positive and negative backscatter changes, due to the fact that there exist both increased and decreased backscatter changes in the fire related areas. In the logRt_abs maps, as shown in the first row in Fig. 6, are the false l)._{VH}l, B = $|\Delta \beta_{VV}|$, G = $|\Delta \beta_{VH}$ color composite (R = $|\Delta \beta|$

Figure 6



SAR-based results on the Camp fire. logRt_abs is the false color I], while the second row shows $_{VH}$ I, $|\Delta\beta_{VV}|$, $|\Delta\beta_{VH}|$ composite with $[|\Delta\beta|]$. The third $_{VH}$, k_{VV} , k_{VH} the false color composite of kmap with [k row shows the burn confidence map predicted by CNN, and the fourth row lists the corresponding binary burn map, marked with CNN burnMap. CNN_mrg is the accumulated burn map by keeping all burn map detected CNN before the considering date, while CNN_tsc_mrg are produced with time series correction on the same orbit, following the merging operation same as CNN_mrg. The bottom row shows the overlayed maps that lay CNN_mrg map over , $G = {}_{2}$ the S2-based false color map with composite [R = SWIR | SWIR | SWIR |

Full size image

Table 4 summarizes the quantitative analysis of the SAR-based wildfire progression mapping results, and these statistics are based on 10,000 samples randomly selected from burnt areas and unburnt areas respectively. With kmap, both VH and VV reach a very high Recall value but a low Precision value, indicating that both of them have a very low false negative rate and high false positive rate. By combining VH and VV together, kmap achieves a much higher precision without a significant decrease in Recall, resulting in the increase in OA (73.05%), Kappa (0.4609) and F1 (0.6339). By applying the proposed CNN-based framework using both VH and VV data, CNN_mrg can achieve a significant improvement in Precision with a minor decrease (0.3%) in Recall, leading to 88.09% in OA, 0.7618 in Kappa and 0.8666 in F1 score. By exploiting TSC, CNN_tsc_mrg can reduce the noisy pixels very well, but the accuracy decreases slightly.

higher imaging frequency. The logRt-based progression maps showed that the VV and VH backscattering have similar sensitivity to changes caused by fire, thus the burnt areas appear white. However, they have very different responses to changes caused by agricultural activities. While VH increases slightly, VV decreases significantly over the agricultural areas (in green). Similar to a wildfire event, the agricultural activities may cause a significant decrease in VV backscattering, which would result in false alarms. Owning to the fact that the agricultural fields often have a high standard deviation in the -historical time series, kmap can suppress the agricultural activities related changes better than log ratio, as shown in the second row. Trained with samples from the binarized kmap, the CNN-based framework can highlight the burnt areas and suppress false alarms due to agricultural activities, as shown in CNN_burnConf and CNN_burnMap. CNN_mrg and CNN_tsc_mrg show the merged results of the burnt areas without or with TSC respectively. The bottom row shows the visual comparison between optical images and SAR-based results, which indicate that SAR data has the potential to detect most of the burnt areas, but some low burn severity areas without structural changes may be missed.

Figure 7

2019	
logRt	SECULO SECU
kmap	Control of the Contro
CNN burnConf [0, 1] Otsu	The state of the s
CNN burnMap {0, 1}	A comment
CNN_mrg	
CNN_ tsc_mrg	
CNN_mrg _overlay	O CONTRACTOR OF THE PARTY OF TH

$_{1}F$	Kappa	OA	Recall	Precisi	Seg.	Metho	Data	Sat.
				on		d		
0.4534	0.2925	64.63	99.69	29.34	>2	kmap	VH	S1
		%	%	%				
0.3518	0.2121	60.61	99.21	21.38			VV	
		%	%	%				
0.6339	0.4609	73.05	98.77	46.67	>2	kmap	VH,	
		%	%	%			VV	
8666.0	7618.0	.88	98.47	.77	Otsu	CNN_	VH,	
		09%	%	38%		mrg	VV	
0.8028	0.6705	83.53	.99	67.09		CNN_t		
		%	94%	%		sc_mr		
						g		

استنتاج

In this paper, we evaluated Senitnel-1 SAR time series for near real-time wildfire progression monitoring using a novel and fully automatic deep learning framework based on CNN. The analysis of SAR temporal backscatter profiles showed that significant differences between burnt forest and grassland can be observed in both the Elephant Hill Fire and the Camp -Fire sites (except C-VH over the Camp Fire site). The CNN based deep learning framework performed much better than log-ratio based kmap in detecting burnt areas, achieving a significant improvement in Kappa over these three study areas: (0.11 for the Elephant Hill Fire, 0.27 for the Camp Fire -and 0.30 for the Chuckegg Creek Fire, respectively). By fine tuning with local data, we demonstrate the proposed CNN framework is effective in monitoring the progressions of three large wildfires in different geographic regions in various topographic conditions. Additional studies are planned to further demonstrate the transferability of the CNN framework to other wildfire events via pixel-wise network forward

SAR-based results on the Chuckegg Creek Fire (2019). logRt is the], while the second row_VH, $\Delta\beta_{VV}$, $\Delta\beta_{VH}$ false color composite with [$\Delta\beta$]. The $_{VH}$, k_{VV} , k_{VH} shows the false color composite of kmap with [k third row shows the burn confidence map predicted by CNN, and the fourth row lists the corresponding binary burn map, marked with CNN burnMap. CNN_mrg is the accumulated burn map by keeping all burn map detected CNN before the considering date, while CNN_tsc_mrg are produced with time series correction on the same orbit, following the merging operation same as CNN_mrg. The bottom row shows the overlayed maps that lay CNN_mrg map over , $B={}_1$, $G=SWIR_2$ the S2-based false color map with [R=SWIR]. $_2SWIR$

propagation. By exploiting all the available SAR data acquired before the wildfire event to characterize the area in terms of backscatter variations due to different environmental conditions, the time series based anomaly detection method is effective in producing coarse burnt area maps that are essential for automatic training of the CNN framework. This research is the first attempt on wildfire progression monitoring using SAR time series and deep learning in challenging topographic conditions. The findings demonstrates that, using a fully automatic deep learning framework, spaceborne SAR data can play a significant role for real-time wildfire progression monitoring when the data becomes available at daily and hourly intervals with the launches of RADARSAT Constellation Missions and SAR CubeSat constellations.

CNN-based Online Learning Framework for Near Real-Time Wildfire Monitoring.

IF: 4.176 | IC Value: 78.46

Methodology

Full size image

Log-ratio based change measurement

To detect changes caused by the wildfire. comparison of preand post-fire SAR images is performed. For each new SAR
image acquired after the start of the wildfire, a pre-fire image
is selected as a master image for each available ascending
(ASC) or descending (DSC) orbit. By applying log-ratio
operator on the master (pre-fire) and slave (after the start of
-the fire) image, a change map can be derived for C-VV and C
VH respectively, and the corresponding log-ratio time series
can be established. The optimal master image is selected
taking into account both minimizing the seasonal effects and
-avoiding master images acquired after heavy rain events. Log
Ratio based change measurement is defined accordingly with
the following formula:

 $\beta r=10log10(\beta mr\beta sr)=10log10(\beta mr)-10$

r)

 $\Delta\beta$ r=10log10(β rm β rs)=10log10(β rm)-10log10(β rs)

(3)

} denote the corresponding orbit ν , DSC- μ {ASC- \in rwhere direction (ASC or DSC) and relative start orbit number is the radar backscattering β , and ν or μ (

The main goal of the methodology is to develop a novel and fully automatic procedure based on a deep learning framework that utilizes every new Sentinel-1 SAR image acquired during -the wildfire event to monitor the fire progression in near real time. When a wildfire occurs, pre-fire SAR dense time series of the study area are collected from the archive and new SAR images are acquired in near real-time during the wildfire event. In particular, the proposed method has two innovative aspects, one is to exploit all available SAR data acquired before the wildfire event to characterize the area in terms of SAR backscatter variations due to different environmental conditions (e.g., seasonal effect, different land cover, weather conditions, etc.) while the other is to automatically train an implicit deep learning framework to estimate the changes in the SAR images acquired during the wildfire. The -methodology includes four major processing steps. First, log ratio of the pre-fire and post-fire SAR images is performed to detect changes caused by wildfire. Then the coarse binary map of burnt and unburnt areas is generated using a time series based anomaly detection technique. Using training samples automatically generated from the coarse binary change map, the CNN is trained and fitted to refine the burnt area detection and to generate the burnt confidence maps. The last step is to binarize the confidence maps using the Otsu automatic thresholding approach and to combine the individual wildfire progression maps progressively to improve their reliability and consistency. The over wew of the methodology is presented in Fig. 8. In the following sub-sections, a full description of the different steps is reported.

Figure 8

IF: 4.176 | IC Value: 78.46

I i,()

 $\geq k0Ik(i,j) < k0$ $I(i,j) = \{1, Ik(i,j) \ge k00, Ik(i,j) < k0\}$ represent pre-fire (master) and post-fire (slave) s and mvalue, image, respectively. By applying log-ratio on the master and can be derived, which β slave images, the change map Δ estimates the difference degree between master and slave are subsequently binarized using β images. The change map Δ the StdDev map as a reference estimation of the regular are σ and β oscillation of the SAR backscatter. Hereafter, Δ for convenient [ab] compact σ and β rewritten as Δ mathematical notation.

Time series based anomaly detection

Based on the pre-fire SAR time series, the corresponding mean and standard deviation (StdDev) are computed with respect to every pixel, forming a mean map and a StdDev are σ map. Over the same study area, the StdDev maps computed based on the historical SAR time series for ASC and DSC orbit respectively, including both VH and VV polarizations. The StdDev maps estimate the normal variance of SAR backscatter with seasonal changes over time, which would provide a pixel-wise reference level for different land cover types in the study area.

map can be transformed into a ${}_{k}IAs$ illustrated in Eq. (6), the , which means the pixels will $_0k$ with a threshold *I*binary map be considered as abnormal ones (i.e., burnt pixels) if they are value in the estimated log-ratio map, ₀klarger than the otherwise, they will be taken as the normal ones, i.e., unburnt = 2 is a good trade-off between detecting $_0k$ pixels. In practice, abnormal changes and suppressing noise. The produced binary maps are the main input in the next CNN refinement step as reference data to automatically select the training samples.

Deep learning-based burnt area refinement

select burnt and unburnt samples for training a CNN model $(i,j) = \sum Nt = 1 (\beta t(i,j) - \beta^-(i,j)) 2N - 1$ As shown in Fig. 8, we use the binary logRt map time series to detect burnt area automatically. By iterating over the available dates, each image is stacked with the corresponding master image and StdDev map in the same orbit, and the DEM products such as elevation, slope and aspects can also be stacked on them. The same number of training samples are randomly chosen from the burnt areas and unburnt areas identified by the log-ratio algorithm with StdDev binarization, and these training samples are stored into a database, used to train a CNN model to further refine the burnt areas. In the testing phase, when the image stack is fed into this CNN model, the corresponding burnt area mapping will be generated automatically.

The CNN framework is designed to produce a confidence -map characterized by a bi-modal distribution of burn and un) denotes the learnable deep network for $\theta(\mathbf{F}$ burnt pixels. Let of OliOildetecting burnt areas, we can derive the output 1) $\theta(F)$ in network $\theta(F)$ layers by forward passing patch $\theta(F)$ the first is the total number of network L), where $\theta(^{L}\mathbf{F}(short \text{ for }$ in Eq. (7). Slayers), and the forward passing is denoted as

$$\begin{split} \sum Nt = & 1(\beta t(i,j) - \beta^{-}(i,j)) 2N - 1 \\ & --- - - \sqrt{} \\ & \sigma(i,j) = \sum t = & 1N(\beta t(i,j) - \beta^{-}(i,j)) 2N - 1 \end{split}$$

(4)

represents the mean image over the available $\beta^-\beta^-$ where SAR time series on the same orbit, and the length is denoted , i.e., the total number of available images acquired on the Nas same orbit.

$$(i,j)$$
Ik $(i,j)=|\Delta\beta(i,j)|\sigma(i,j)$

(5)

In order to detect the abnormal variance caused by wildfire |1,j,i| from $|\Delta \sigma$ events, a k-Map can be computed by dividing estimates the times that _kIas shown in Eq. 5. The k-map for each pixel in σ) is larger than the corresponding j, $i(\beta | \Delta)$ the study area: a higher value in the k-Map means it is abnormal variation corresponding to a higher probability of changes.

 $Oli=Pi\otimes Fl(\theta)Oil=Pi\otimes Fl(\theta)$

(6)

IF: 4.176 | IC Value: 78.46

collects the θ), and $\theta(\mathbf{F}_{\mathbf{k}})$ avers of l) denotes the first $\theta(l^{\mathbf{k}})$ where . Specially, the input L=0, 1, 2, ..., l, $\theta({}^{l}\mathbf{F}$ weights and bias of

$$(\theta) = 1n\sum_{i=1}^{n} \|y^{i} - yi\| 22 + \lambda \|\theta\| 22$$

$$\ell(\theta) = 1n\sum_{i=1}^{n} \|y^{i} - yi\| 22 + \lambda \|\theta\| 22$$

$$\text{Specially, the input } L=0, 1, 2, ..., \ell), \theta \text{ Fweights and bias of relationship can be formulated as: } 0, \text{ and } 0, \text{ and } 0 \text{ or the formulated as: } 0 \text{ or the for$$

(9)

is the learn-able θ is the number of training samples, nwhere network parameter over all layers, including weights and bias, controls the weight decay rate. In our problem (012a14+b1) $0il=\delta(W1*0il-1+b1)$

= 0.001. Once trained, the corresponding burn confidence λ set map can be obtained, which can be used to update the binary logRt time series for next training. Like this, the Pseudo label updating can contribute to providing more reliable ones, but it is not necessary. Moreover, Digital Elevation Model (DEM) products can be integrated to take topography into consideration as additional input layers.

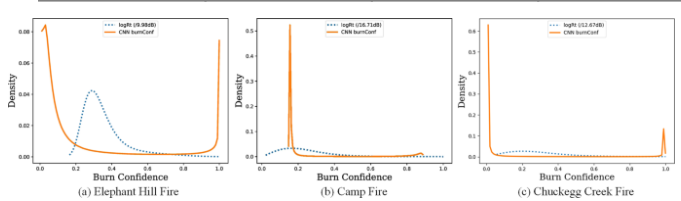
CNN BurnConf maps: binarization and time series merging

maps, CNN burnConfThe outputs of the CNN refinement are where the pixel values are ranging from 0 to 1 and they are proportional to the probability that each pixel represent a burnt area (0: unburnt, 1: burnt). The main advantage of using the proposed CNN framework is that the differences in term of backscatter variation between burnt and unburnt pixel are represented by a clear bi-modal distribution (see Fig. 9) with respect to unimodal distribution of the log-ratio based results (scaled to [0, 1] by dividing the maximum). Consequently, maps are easy to be binarized using an CNN burnConfthe .52Otsu automatic thresholding technique

Figure 9

-th layer l represent weights and bias of lb and lWwhere . ³⁸ is the ReLU activation function δ), respectively, and θ (Fin Table 5 lists the CNN architecture used, it has 18 layers of neural networks, and each convolutional layer is followed by a CNN ReLU activation (sigmoid for the last layer). The map is derived by applying the sigmoid activation burnConf on the output of the last layer, since burnt area detection is actually a binary classification problem, and the sigmoid activation is a good choice to scale the predicted confidence into the range [0, 1].

Out	put	Operation	Layer No.
Test	Train		
$7 \times (w + 54) \times$	$7 \times 55 \times 55$	_	0 (input)
(h + 54)			
$20 \times (w + 52)$	$20 \times 53 \times 53$	20@3 × 3Conv	1
\times (h + 52)		+ ReLU	
$20 \times (w + 16)$	$20 \times 17 \times 17$	20@7 × 7Conv	2–8
\times (h + 16)		+ ReLU	
$20 \times w \times h$	$20 \times 1 \times 1$	20@3 × 3Conv	9–17
		+ ReLU	
$2 \times w \times h$	$2 \times 1 \times 1$	2@1 × 1Conv	18
		+ Sigmoid	



), a CNN-based non-linear iy, iPWith randomly sampled data () can be learnt for highlighting the burnt θ (Fchange indicator areas based on the SAR data. The predicted burn confidence

V^i∕€ctor

(8)

 $R2 \times 1y^{i} \in R2 \times 1$ can be derived by squeezing $OLi = R2 \times 1y^{i}$

CNN Comparison distribution among maps on the finding to the finding t

. Therefore, $OiL = Pi \otimes F(\theta) \in R2 \times 1 \times 1 \times 1 \\ \text{the loss function can be formulated as:}$

Full size image

To produce more reliable and consistent fire progression maps, the binary wildfire progression maps at different stages

are combined using two different methods. The first method is for near-real time wildfire progression monitoring and it simply combines the new wildfire progression map with the previous ones to generate the latest burnt area map. This method does not use the later burnt map to improve the results of the previous ones. This method has been investigated to highlight the potential of the SAR-based CNN framework for near real-time wildfire monitoring. The second method is a post-processing step that uses all the generated binary maps to update the fire progression maps exploiting the available multitemporal information. The method reduces the noise using a gaussian temporal filtering of the produced burnt map time series and it can be used to obtain a more reliable delineation of the fire progression for post-fire analysis (i.e. calibration of fire progression models).

Data availability

The datasets generated during and/or analysed during the current study are available from the corresponding author on reasonable request.

ref_str

- Yue, X., Mickley, L. J., Logan, J. A. & Kaplan, J. O. Ensemble projections of wildfire activity and carbonaceous aerosol concentrations over the western United States in the mid-21st century. Atmos. Environ. 77,
- 767-780, https://doi.org/10.1016/j.atmosenv.2013.06.003 (2013).
- Schroeder, W. et al. Validation of GOES and MODIS active fire detection products using ASTER and ETM+ data. Remote. Sens. Envir on., https://doi.org/10.1016/j.rse.2008.01.005 (2008).
 - Schroeder, W., Oliva, P., Giglio, L. & Csiszar, I. A. The New VIIRS 375 m active fire detection data product: Algorithm description and initial assessment. Remote. Sens. Environ. 143, 85_96, https://doi.org/10.1016/j.rse.2013.12.008 (2014).
 - -Wulder, M. A. et al. Characterizing boreal forest wildfire with multitemporal Landsat and LIDAR data. Remote. Sens. Environ. 113, 1540–1555, https://doi.org/10.1016/j.rse.2009.03.004 (2009).
 - Quintano, C., Fernández-Manso, A. & Fernández-Manso, O. Combination of Landsat and Sentinel-2 MSI data for initial assessing of burn severity. Int. J. Appl. Earth Obs. Geoinf. 64, 221–225, https://doi.org/10.1016/j.jag.2017.09.014 (2018).
 - -Crowley, M. A., Cardille, J. A., White, J. C. & Wulder, M. A. Multi sensor, multi-scale, Bayesian data synthesis for mapping within-year wildfire progression. Remote. Sens. Lett. 10,
 - 302–311, https://doi.org/10.1080/2150704X.2018.1536300 (2019).
 - Chuvieco, E. et al. Historical background and current developments for mapping burned area from satellite Earth observation. Remote.

 Sens. Environ. 225,
 - 45-64, https://doi.org/10.1016/j.rse.2019.02.013 (2019).
- Engelbrecht, J., Theron, A., Vhengani, L. & Kemp, J. A Simple Normalized Difference Approach to Burnt Area Mapping Using Multi Polarisation C-Band SAR. Remote. Sens. 9, 764, https://doi.org/10.3390/rs9080764 (2017).
 - French, N. H., Bourgeau-Chavez, L. L., Wang, Y. & Kasischke, E. S. Initial observations of Radarsat imagery at fire-disturbed sites in

- interior Alaska. Remote. Sens. Environ. 68, 89–94, https://doi.org/10.1016/S0034-4257(98)00094-7 (1999).
 - Goodenough, D. G. et al. Mapping fire scars using Radarsat-2 polarimetric SAR data. Can. J. Remote. Sens. 37, 500–509, https://doi.org/10.5589/m11-060 (2012).
- Imperatore, P. et al. Effect of the Vegetation Fire on Backscattering:

 An Investigation Based on Sentinel-1 Observations. IEEE J. Sel. Top.

 Appl. Earth Obs. Remote. Sens. 10,
- 4478–4492, https://doi.org/10.1109/JSTARS.2017.2717039 (2017).

 Mouillot, F. et al. Ten years of global burned area products from spaceborne remote sensing-A review: Analysis of user needs and recommendations for future developments. Int. J. Appl. Earth Obs. Geoinf. 26, 64–79, https://doi.org/10.1016/j.jag.2013.05.014 (2014).
- Polychronaki, A., Gitas, I., Veraverbeke, S. & Debien, A. Evaluation of ALOS PALSAR Imagery for Burned Area Mapping in Greece Using Object-Based Classification. Remote. Sens. 5, 5680–5701, https://doi.org/10.3390/rs5115680 (2013).
- Stroppiana, D. et al. Integration of optical and SAR data for burned area mapping in Mediterranean Regions. Remote. Sens. 7, 1320–1345, https://doi.org/10.3390/rs70201320 (2015).
- Tanase, M. A., Pérez-Cabello, F., De La Riva, J. & Santoro, M. TerraSAR-X data for burn severity evaluation in mediterranean forests on sloped terrain. IEEE Trans. Geosci. Remote. Sens. 48, 917–929, https://doi.org/10.1109/TGRS.2009.2025943 (2010).
- Tanase, M. A. et al. Sensitivity of X-, C-, and L-band SAR backscatter to burn severity in Mediterranean pine forests. IEEE Trans. Geosci.

 Remote. Sens. 48,
 - 3663-3675, https://doi.org/10.1109/TGRS.2010.2049653 (2010).
- Bourgeau-Chavez, L., Kasischke, E., Brunzell, S., Mudd, J. & Tukman, M. Mapping fire scars in global boreal forests using imaging radar data. Int. J. Remote. Sens. 23,
- 4211–4234, https://doi.org/10.1080/01431160110109589 (2002).

 Gimeno, M., San-Miguel-Ayanz, J. & Schmuck, G. Identification of burnt areas in Mediterranean forest environments from ERS-2 SAR time series. Int. J. Remote. Sens. 25,
- 4873–4888, https://doi.org/10.1080/01431160412331269715 (2004).
- Verhegghen, A. et al. The Potential of Sentinel Satellites for Burnt Area Mapping and Monitoring in the Congo Basin Forests. Remote. Sens. 8, 986, https://doi.org/10.3390/rs8120986 (2016).
- Kurum, M. C-Band SAR Backscatter Evaluation of 2008 Gallipoli Forest Fire. IEEE Geosci. Remote. Sens. Lett. 12,
- $1091-1095, https://doi.org/10.1109/LGRS.2014.2382716\ (2015).$
- Siegert, F. & Ruecker, G. Use of multitemporal ERS-2 SAR images for identification of burned scars in south-east Asian tropical rainforest. Int. J. Remote. Sens. 21,
 - 831-837, https://doi.org/10.1080/014311600210632 (2000).
- Menges, C., Bartolo, R., Bell, D. & Hill, G. E. The effect of savanna fires on sar backscatter in northern australia. Int. J. Remote. Sens. 25, 4857–4871, https://doi.org/10.1080/01431160410001712945 (2004).
- Huang, S. & Siegert, F. Backscatter change on fire scars in Siberian
 boreal forests in ENVISAT ASAR wide-swath images. IEEE Geosci.
 Remote. Sens. Lett. 3,
 - 154-158, https://doi.org/10.1109/LGRS.2005.860483 (2006).
 - Belenguer-Plomer, M. A., Tanase, M. A., Fernandez-Carrillo, A. & Chuvieco, E. Burned area detection and mapping using sentinel-1 backscatter coefficient and thermal anomalies. Remote. Sens. Environ. 233,
 - 111345, https://doi.org/10.1016/j.rse.2019.111345 (2019).
- Reiche, J., de Bruin, S., Hoekman, D., Verbesselt, J. & Herold, M. A Bayesian approach to combine Landsat and ALOS PALSAR time series for near real-time deforestation detection. Remote. Sens. 7, 4973–4996, https://doi.org/10.3390/rs70504973 (2015).
- Reiche, J., Verbesselt, J., Hoekman, D. & Herold, M. Fusing Landsat and SAR time series to detect deforestation in the tropics. Remote.

 Sens. Environ. 156,
 - 276-293, https://doi.org/10.1016/j.rse.2014.10.001 (2015).
- Reiche, J., Hamunyela, E., Verbesselt, J., Hoekman, D. & Herold, M.
 Improving near-real time deforestation monitoring in tropical dry
 forests by combining dense Sentinel-1 time series with Landsat and
 ALOS-2 PALSAR-2. Remote. Sens. Environ. 204,
 - 147–161, https://doi.org/10.1016/j.rse.2017.10.034 (2018).

 Ban, Y. Multitemporal remote
 - sensing, https://doi.org/10.1007/978-3-319-47037-5 (2016).
 - DeVries, B., Verbesselt, J., Kooistra, L. & Herold, M. Robust monitoring of small-scale forest disturbances in a tropical montane forest using Landsat time series. Remote. Sens. Environ. 161,

1. NOAA Natl. Centers for

- Environ. Inf., https://doi.org/10.7289/V51V5BWQ (2014).
- Ashouri, H. et al. PERSIANN-CDR: Daily precipitation climate data record from multisatellite observations for hydrological and climate studies. Bull. Am. Meteorol. Soc. 96,

69-83, https://doi.org/10.1175/BAMS-D-13-00068.1 (2015).

- -Funk, C. et al. The climate hazards infrared precipitation with stations a new environmental record for monitoring extremes. Sci. Data 2, 150066, https://doi.org/10.1038/sdata.2015.66 (2015).
 - Otsu, N. A threshold selection method from gray-level histograms. IEEE Trans. Syst. Man, Cybern. 9,
 - 62–66, https://doi.org/10.1109/TSMC.1979.4310076 (1979).
 - Kingma, D. P. & Ba, J. Adam: A method for stochastic
 - optimization. arXiv preprint, https://arxiv.org/abs/1412.6980 (2014).

- 107-121, https://doi.org/10.1016/j.rse.2015.02.012 (2015).
- Hansen, M. C. et al. High-Resolution Global Maps of. Sci. 850, 2011–2014, https://doi.org/10.1126/science.1244693 (2013).
- Raspini, F. et al. Continuous, semi-automatic monitoring of ground deformation using Sentinel-1 satellites. Sci. Rep. 8,
 - $7253, https://doi.org/10.1038/s41598-018-25369-w\ (2018). \\$
- Zhu, Z. & Woodcock, C. E. Continuous change detection and classification of land cover using all available Landsat data. Remote.

 Sens. Environ. 144,
 - 152-171, https://doi.org/10.1016/j.rse.2014.01.011 (2014).
- Yousif, O. & Ban, Y. Improving SAR-based urban change detection by combining MAP-MRF classifier and nonlocal means similarity weights. IEEE J. Sel. Top. Appl. Earth Obs. Remote. Sens. 7, 4288–4300, https://doi.org/10.1109/JSTARS.2014.2347171 (2014).
 - Bruzzone, L. & Prieto, D. F. Automatic analysis of the difference image for unsupervised change detection. IEEE Trans. Geosci.

 Remote. Sens. 38,
 - 1171-1182, https://doi.org/10.1109/36.843009 (2000).
- Bazi, Y., Bruzzone, L. & Melgani, F. An unsupervised approach based on the generalized Gaussian model to automatic change detection in multitemporal SAR images. IEEE Trans. Geosci. Remote. Sens. 43, 874–887, https://doi.org/10.1109/TGRS.2004.842441. (2005).
- Bovolo, F. & Bruzzone, L. A detail-preserving scale-driven approach to change detection in multitemporal SAR images. IEEE Trans.

 Geosci. Remote. Sens. 43,
 - 2963–2972, https://doi.org/10.1109/TGRS.2005.857987 (2005).
 - Bovolo, F. & Bruzzone, L. An adaptive thresholding approach to multiple-change detection in multispectral images. In Proc. of the IEEE Int. Geosci. and Remote Sens. Symp.,
 - 233–236, https://doi.org/10.1109/IGARSS.2011.6048935 (IEEE, 2011).
- Krizhevsky, A., Sutskever, I. & Hinton, G. E. Imagenet classification with deep convolutional neural networks. In Adv. in Neural Inf. Process. Syst.
 - 1097-1105, https://doi.org/10.1145/3065386 (2012).
- He, K., Zhang, X., Ren, S. & Sun, J. Deep residual learning for image recognition. In Proc. of the IEEE Conf. on Comput. Vision and Pattern Recognit.,
 - 770-778, https://arxiv.org/abs/1512.03385v1 (2016).
 - Redmon, J., Divvala, S., Girshick, R. & Farhadi, A. You only look once: Unified, real-time object detection. In Proc. of the IEEE Conf. on Comput. Vision and Pattern Recognit.,
 - 779-788, https://doi.org/10.1109/CVPR.2016.91 (2016).
- Long, J., Shelhamer, E. & Darrell, T. Fully convolutional networks for semantic segmentation. In Proc. of the IEEE Conf. on Comput. Vision and Pattern Recognit
 - 3431-3440, https://doi.org/10.1109/TPAMI.2016.2572683 (2015).
- Gong, M., Zhao, J., Liu, J., Miao, Q. & Jiao, L. Change detection in synthetic aperture radar images based on deep neural networks. IEEE Trans. Neural Netw. Learn. Syst. 27,
 - 125-138, https://doi.org/10.1109/TNNLS.2015.2435783 (2015).
- Gong, M., Yang, H. & Zhang, P. Feature learning and change feature classification based on deep learning for ternary change detection in SAR images. ISPRS J. Photogramm. Remote. Sens. 129,
 - 212–225, https://doi.org/10.1016/j.isprsjprs.2017.05.001 (2017).
- Zhu, X. X. et al. Deep learning in remote sensing: A comprehensive review and list of resources. IEEE Geosci. Remote. Sens. Mag. 5, 8–36, https://doi.org/10.1109/MGRS.2017.2762307 (2017).
- Zhang, P., Gong, M., Zhang, H., Liu, J. & Ban, Y. Unsupervised difference representation learning for detecting multiple types of changes in multitemporal remote sensing images. IEEE Trans. Geosci.

 Remote. Sens. 57,
 - 2277-2289, https://doi.org/10.1109/TGRS.2018.2872509 (2018).
- Sentinel-1 mission, https://sentinel.esa.int/web/sentinel/missions/sentin el-1 Accessed Jun 25 (2019).
 - Gorelick, N. et al. Google Earth Engine: Planetary-scale geospatial analysis for everyone. Remote. Sens. Environ. 202, 18–27, https://doi.org/10.1016/j.rse.2017.06.031 (2017).
 - Miller, J. D. et al. Calibration and validation of the relative differenced normalized burn ratio (rdnbr) to three measures of fire severity in the sierra nevada and klamath mountains, california, usa. Remote. Sens. Environ. 113,
 - 645-656, https://doi.org/10.1016/j.rse.2008.11.009 (2009).
 - Sorooshian, S. et al. NOAA Climate Data Record (CDR) of Precipitation Estimation from Remotely Sensed Information Using Artificial Neural Networks (PERSIANN-CDR), Version 1, Revision



IJSURP Publishing Academy International Journal Of Scientific And University Research Publication Multi-Subject Journal

Editor.

International Journal Of Scientific And University Research Publication



www.ijsurp.com